Ceramics International xxx (xxxx) xxx

Contents lists available at ScienceDirect

Ceramics International

journal homepage: www.elsevier.com/locate/ceramint

Wideband electromagnetic wave absorption by tuning morphology and layer arrangement in Bi-layer absorber based on doped $SrFe_{12}O_{19}$ nanocomposite powders

Jian Huang [a,*], Isabelle Huynen [b,**], Sadok Mehrez [c,d], Ibrahim Mahariq [e], Mohamed Fayed [e], Ahmed Ashour [f]

[a] Xijing University, Xi'an, Shaanxi, 710123, China
[b] ICTEAM Institute, ELEN Division, Place du Levant 3, Louvain-la-Neuve, B-1348, Belgium
[c] Department of Mechanical Engineering, College of Engineering at Al Kharj, Prince Sattam Bin Abdulaziz University, 16273, Saudi Arabia
[d] Department of Mechanical Engineering, University of Tunis El Manar, ENIT, BP 37, Le Belvédère, 1002, Tunis, Tunisia
[e] College of Engineering and Technology, American University of the Middle East, Kuwait
[f] Engineering Maths and Physics Department, Faculty of Engineering and Technology, Future University in Egypt New Cairo, 11835, Egypt

ARTICLE INFO

Keywords:
Doped $SrFe_{12}O_{19}$
Microwave absorption
Bi-layer absorber
Solvothermal

ABSTRACT

The main parameters for achieving the optimum microwave dissipation performance in bi-layer absorbers are micromorphological characteristics, filler content composition, and layer configurations. In this research, two different doped strontium hexaferrite powders with $SrFe_{10}Al_2O_{19}$ (PSrAl) and $SrFe_{10}CoTiO_{19}$ (CSrCoTi) chemical formulas were prepared through a solvothermal method. This study aims to identify optimal absorption conditions for bilayer samples by combining different magnetic compositions with varying ferromagnetic resonance and diverse morphologies with different layer arrangements. Single layer absorber samples comprising PSrAl powder with a polygonal pyramidal particle shape displayed dominating dielectric loss behavior and ferromagnetic resonance at about 11.6 GHz, according to the findings. On the other hand, absorber samples containing CSrCoTi powder with crochet ball like particle morphology, exhibit dominant magnetic loss behavior in the studied frequency range, with ferromagnetic resonance around 8.8 GHz. According to the results of bi-layer absorber samples, superior microwave dissipation performance could be achieved by inserting PSrAl powder in the top layer as a matching layer with 0.5 mm thickness and CSrCoTi powder as an absorbing layer 2 mm-thick. For a bi-layer absorber with a 2.5 mm total thickness The EAB (effective absorption bandwidth) is equal to 3.1 GHz at X-band and the minimum reflection loss is equal to −22 dB. The tuning morphology, which improved impedance matching and absorption properties by increasing the wave propagation path in the sample, synergistic effect between two distinct layers, and overlapping of resonance peaks of two components, is credited with this remarkable microwave absorption feature.

1. Introduction

Microwave absorbing structures (MAS) act as efficient protection against electromagnetic interferences [1,2]. MAS designed for stealth applications reduce the radar cross-section (RCS) of targets assumed to be metallic: an absorbing shield covering them reduces the signal reflected by the target in the direction of the radar [3,4]. This corresponds to the Salisbury screen configuration, widely used for radar communications at X band (8–12.4 GHz) [5]. Reflection below −10 dB can be achieved by dispersing conductive carbon fillers at different concentrations in single as well as multilayer configurations [6,7]. Incorporating magnetic charges into the composite is a good strategy in order to counterbalance the reflective effect of highly conductive charges, [8–11]. An illustration of various research aspects devoted to MAM absorbers can be found in Refs. [12–16].

In this work two different doped strontium hexaferrite powders, $SrFe_{10}Al_2O_{19}$ (PSrAl) and $SrFe_{10}CoTiO_{19}$ (CSrCoTi), were prepared through a solvothermal method. In Ref. [17], an iron-strontium

* Corresponding author.
** Corresponding author.
E-mail addresses: huangjian108@tom.com (J. Huang), isabelle.huynen@uclouvain.be (I. Huynen).

https://doi.org/10.1016/j.ceramint.2022.07.017
Received 20 April 2022; Received in revised form 28 June 2022; Accepted 5 July 2022
Available online 8 July 2022

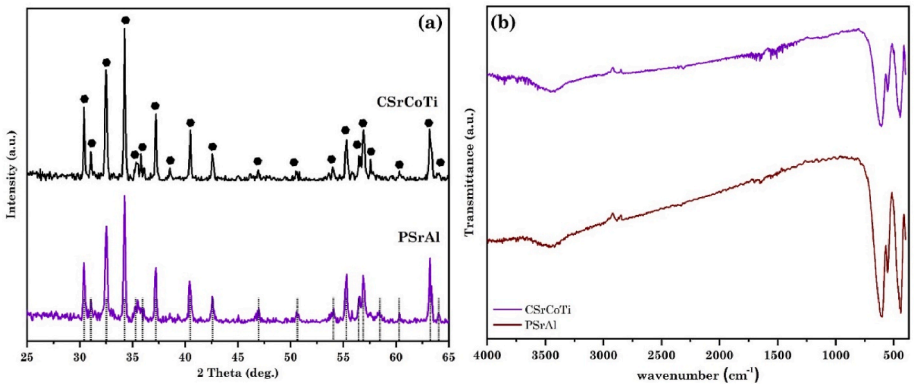

Fig. 1. a) XRD and b) FTIR analysis results of as-prepared powders.

composite slab shows return loss RL = −23 dB at 9.2 GHz for a thickness of 3.5 mm and, and a 10 dB effective absorption bandwidth (EAB) equal to 3.4 GHz. In Ref. [18] hydrothermal method was used to sythezise ultrathin $SrFe_{12}O_{19}$ nanosheets. RL reached a minimum value of - 28.6 dB for EAB = 0.92 GHz and a 3.5 mm thickness. In Ref. [19] sol-gel technique was used to obtain a composite powder with different ratios of strontium and zinc hexaferrites that reaches minimum RL = −37 dB for a thickness of 2.2 mm. In Ref. [20] coprecipitation and in situ polymerization was used for the obtention of reduced graphene oxide/strontium ferrite/polyaniline ternary nanocomposite. The minimum RL value was −45.00 dB at 16.08 GHz with EAB = 5.48 GHz and thickness of 1.5 mm. In Ref. [21] sol-gel technique was used to obtain a composite powder with different ratios of strontium and zinc hexaferrites. The minimum reflection loss reaches −37 dB at X band for a thickness of 2.2 mm. In Ref. [22] combustion was used to prepare a combination of two ternary composites of SrFe10Al2O19/MWCNTs/polypyrrole and Ni0.5Zn0.5Fe2O4/MWCNTs/polypyrole. The composite powder in polyester resin reaches RL = −34.5 dB for a thickness of 3 mm and EAB = 3.05 GHz. In Ref. [23] in situ chemical oxidative method was used to prepare NiCoTi ferrite, SrCoTi ferrite and copper microparticles coated with polypyrrole. The absorber with 20% loading percentage in polyurethane has RL = −24 dB at the matching frequency 9.75 GHz and an EAB = 3 GHz for a thickness of 1.8 mm. Finally, in Ref. [24] cobalt-based MOF/SrFe10CoTiO19/carbon nanofibers reached − 19 dB with EAB = 3.9 GHz in the Ku-band with the thicknesses of only 2.5 mm.

Section 2 in this paper describes the synthesis methods for doped $SrFe_{12}O_{19}$ nanocomposites, and their characterization methods. Section 3 presents XDR, FITR, FESEM and VSM results, and the measurement of their electromagnetic parameters. The reflection losses of $SrFe_{10}Al_2O_{19}$ (PSrAl) and $SrFe_{10}CoTiO_{19}$ (CSrCoTi) are estimated as a function of frequency and for various thicknesses of composite sample and frequency, both for single layer topology or bilayer topology. Section 4 presents the conclusions of the work.

2. Materials and methods

2.1. Synthesis of polygonal-pyramidal shape-like $SrFe_{10}Al_2O_{19}$ (PSrAl)

In this research, nitrate salts ($Sr(NO_3)_2$, $Fe(NO_3)_3.9H_2O$, $Al(NO_3)_3$) were used as raw precursors for synthesizing doped strontium hexaferrite with $SrFe_{10}Al_2O_{19}$ chemical formula. In a typical synthesis and based on the chemical composition, an appropriate amount of the nitrate salts, were completely dissolved in a mix of deionized water and pure ethanol in equivalent ratio. Then, 20% of the raw precursors, ascorbic acid is added to the solution. Following that, the pH is adjusted to 10 by adding a 10 M KOH solution dropwise into the aforementioned solution. The resulted solution was sealed in an autoclave followed by heated in an oven at 200 °C for 15 h. The resulting products were rinsed several times using ethanol and water before being dried and sintered at 1000 °C for 1 h.

2.2. Synthesis of hierarchical crochet ball-like $SrCoTiFe_{10}O_{19}$ (CSrCoTi)

The crochet ball like doped strontium hexaferrite with the chemical formula $SrFe_{10}CoTiO_{19}$ is synthesized using the solvothermal technique. The stoichiometric quantities of reactants (strontium nitrate, iron nitrate, cobalt nitrate, and titanium tetraisopropoxide) were dissolved in ethylene glycol in the first stage, followed by the addition of urea. The urea/ions ratio was fixed to 5. After that, the suspension was poured into an autoclave reactor and heated during 24 h at 210 °C. The precipitate separated from the suspension and, after washing, was dried and sintered at 1000 °C during 3 h.

2.3. Characterizations

Structural and phase constitution of each powder is recorded and evaluated via X-ray diffractometer (XRD: Philips -PW1730 in the range of 2θ = 25–65°) and Fourier-transform infrared spectroscopy (FTIR: Nicolet 380), room temperature magnetic properties is extract via vibrating sample magnetometer (VSM: ADE EV-11), microstructural features were characterized via Field emission scanning electron microscope (FESEM: ZIESS sigma). Microwave absorption performances of single paraffin layers were measured at X-band frequency using a vector network analyzer (VNA: MS4644A).

2.4. Fabrication of single layer absorber samples

First of all, paraffin was molted and heated up-to melting temperature for a moment, and the 20 wt% of the prepared powders were evenly mixed well in it separately. After preparing a single layer sample, the electromagnetic parameters were extracted via VNA test and used as base values for simulating the bi-layer absorber. The best absorption features achievable by tuning the layer arrangement and changing the morphology of the particles is investigated.

3. Results and discussion

3.1. Physico-chemical properties

XRD and FTIR spectra results of PSrAl and CSrCoTi powders are depicted in Fig. 1 (a,b) respectively. The production of a single phase magnetoplumbite M-type $SrFe_{12}O_{19}$ is confirmed by the fact that all indexed peaks fit well with the standard JCPDS card peaks # 24–1207, space group: $P6_3/mmc$ (194) and both powders have almost same diffraction patterns. No impurity can be retraced. It was important to note that a little movement of the peaks in both patterns to lower angles may be attributed to an increase in the lattice parameters. All indexed

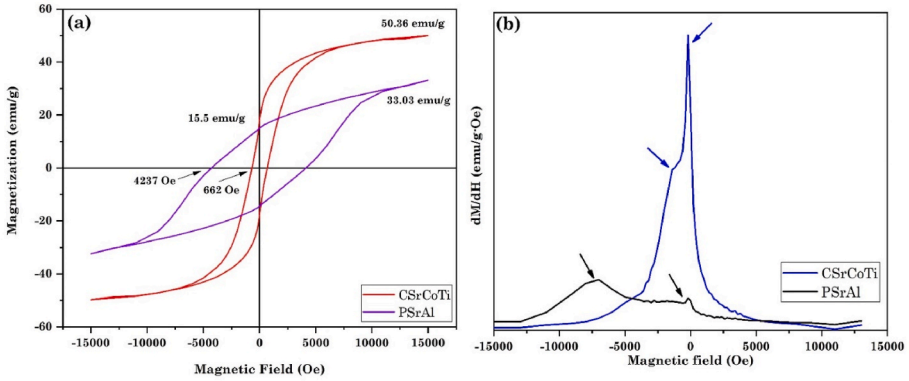

Fig. 2. a) Room temperature magnetic hysteresis loops and b) dM/dH versus H curves of as-prepared powders.

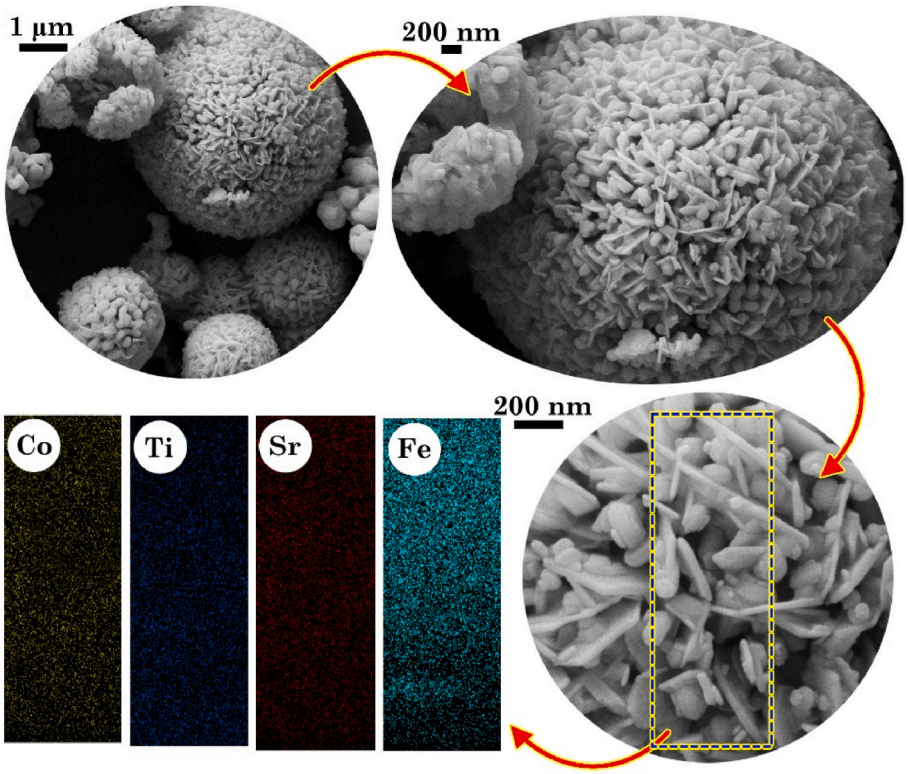

Fig. 3. FESEM images and elemental mapping analaysis results of CSrCoTi samle.

diffraction peaks located at 30.32°, 31.05°, 32.3°, 34.17°, 35.16°, 37.11°, 38.48°, 40.36°, 42.51°, 50.48°, 53.90°, 55.18°, 56.40°, 60.31° and 63.12° match well with the (110), (008), (107), (114), (200), (203), (116), (205), (206), (209), (300), (217), (304), (2,0,12) and (220) crystal planes diffractions. The FT-IR spectra of PSrAl and CSrCoTi powders were captured in the 400-4000 cm^{-1} range using the KBr technique for determining the bond vibration mode. These spectra are shown in Fig. 1b. The stretching vibrations modes of metal-oxygen which correspond to Fe^{3+}-O^{2-} bonds in octahedral, hexahedral and tetrahedral sites in strontium hexaferrite crystal structure were appeared as absorption peaks at 433, 550 and 594 cm^{-1} respectively. These absorptions verify the relevant literature's findings that a M-type hexagonal structure formed.

3.2. Magnetic properties

Fig. 2a and b shows magnetizationn hysteresis loops which are recorded at room temperature within the range of −15000 up to 15000 Oe and interphase exchange for the as-prepared powders, respectively. The substitution of different cations with Fe3+ ions in the crystal structure of strontium hexaferrite is responsible for both samples of the ferrimagentic character and smooth loops in the curves of saturation magnetization (Ms) and coercivity field (Hc). Ms values of the samples of CSrCoTi and PSrAl is 50.36 and 33.03 emu/g, respectively. Notably, both samples' Ms and Hc values are lower than those expected for M-type strontium hexaferrites. One of the possible reasons for the decline in Ms values is the replacement of cations in the crystal structure, which leads to a weakening of the super exchange interaction. The Hc values of the CSrCoTi and PSrAl samples are 662 and 4237 Oe, respectively. For the CSrCoTi and PSrAl samples, respectively, soft magnetic and hard magnetic nature can be shown, which may significantly alter the ferromagnetic resonance of each sample. Additionally, the acquired results in Fig. 2b show that both samples have one strong peak with a little kink that indicates imperfect magnetization reversal, which is

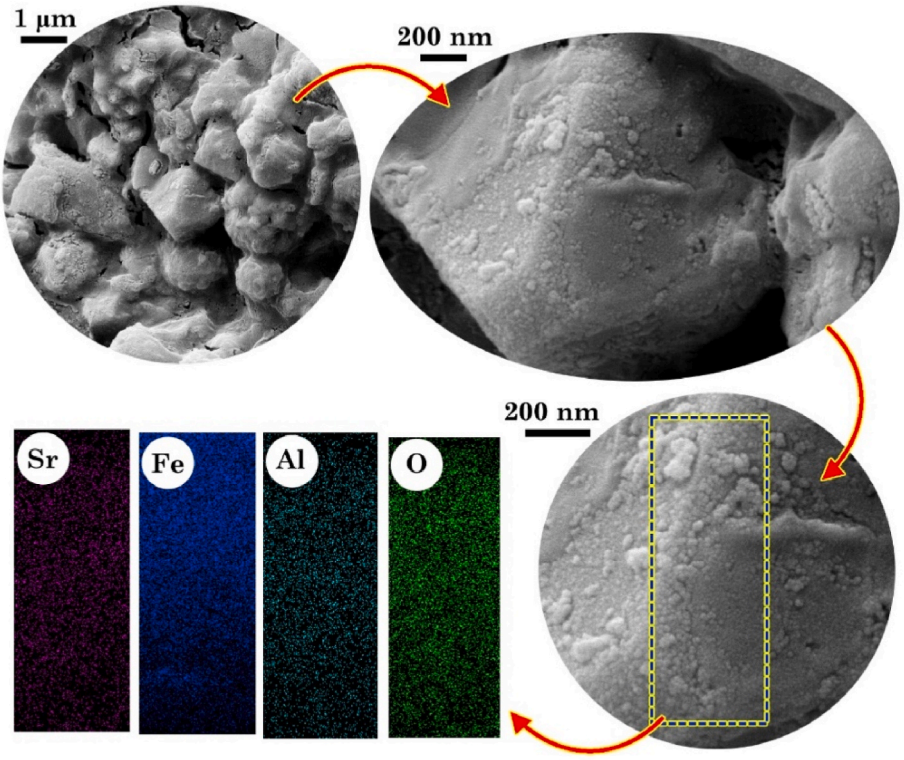

Fig. 4. FESEM images and elemental mapping analaysis results of PSrAl sample.

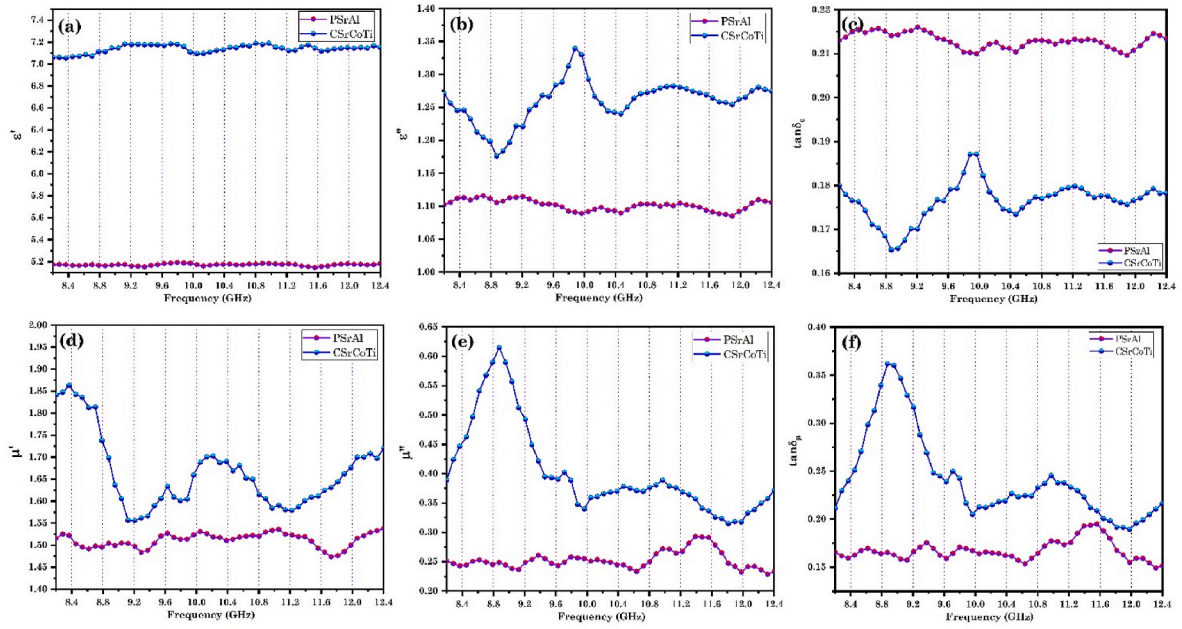

Fig. 5. Dielectric and magnetic parameters of single layer PSrAl and CSrCoTi samples, a) ε′, b) ε″, c) tanδϵ, d) μ′, e) μ″ and f) tanδ$_\mu$.

explained by the morphology of the samples.

3.3. Morphological properties

The elemental maps and FESEM images of the CSrCoTi powder are shown in Fig. 3, where it is evident that the powder has a crochet-like morphology and a rich porosity structure that enhances multi-scattering processes in the particles. The spontaneous assembly of adjacent particles, which leads to the production of three-dimensional particles, is made easier by the addition of ethylene glycol and urea as surfactants in the solvothermal method. The findings of the elemental mapping clearly show that Co, Ti, Sr, and Fe elements are present and are distributed uniformly throughout the processed sample's structure (see Fig. 4).

In Fig. 3, which displays the PSrAl powder's elemental maps and FESEM images, it is clear that the powder has a polygonal pyramidal shape. The results of the elemental mapping conclusively demonstrate that O, Al, Sr, and Fe elements are evenly dispersed throughout the

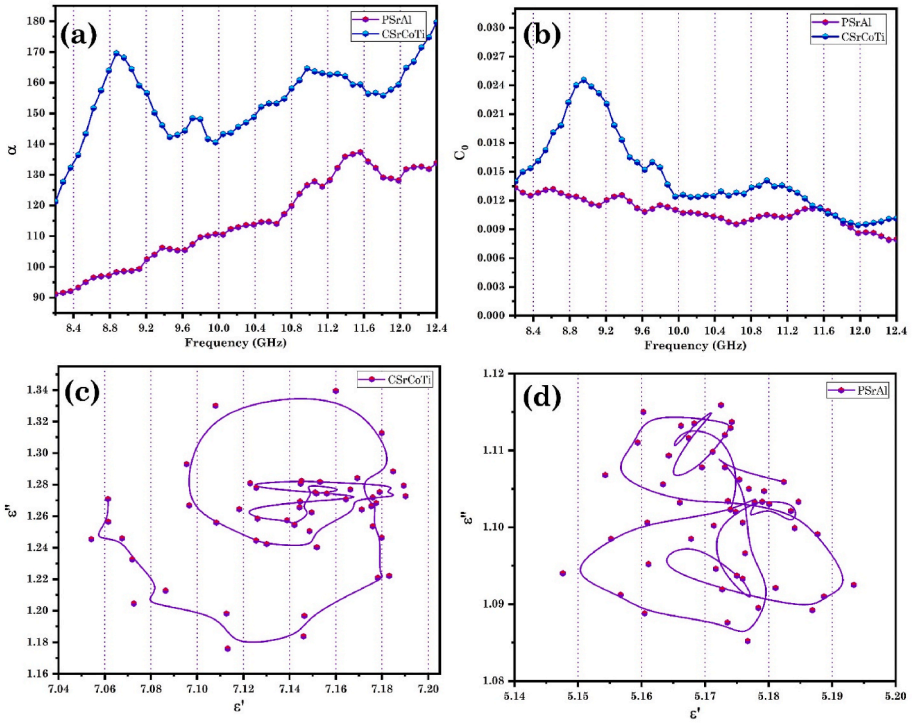

Fig. 6. a) α versus frequency, b) C_0 versus frequency and c,d) Cole-Cole plots 0f the single layer absorber samples.

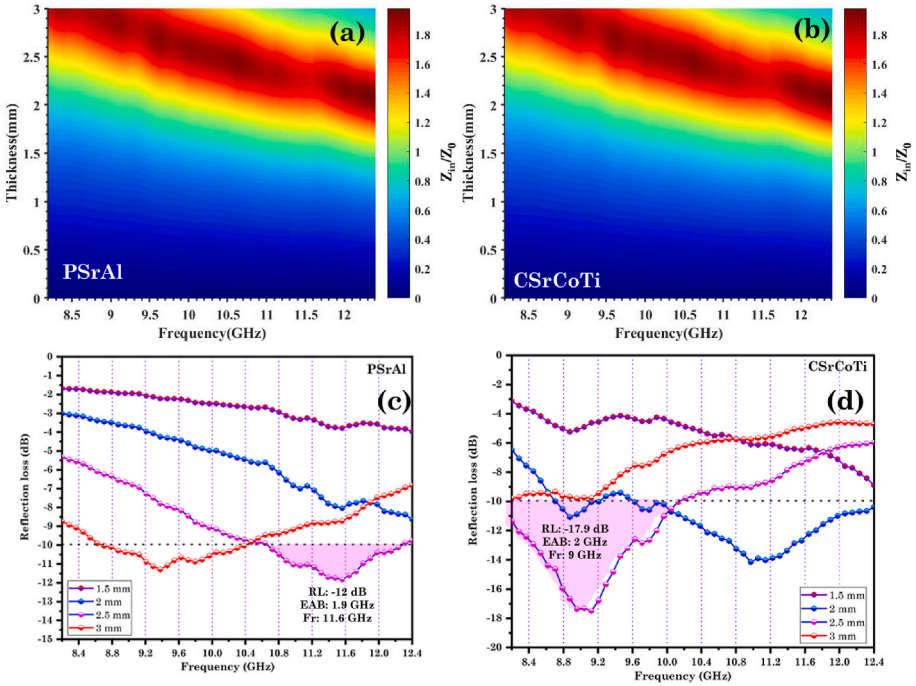

Fig. 7. a,b) Z_{in}/Z_0 contour map versus frequency and thickness (c,d) reflection loss curves versus frequency with different thickness.

structure of the sample.

3.4. Electromagnetic parameters

As explained in section 2.3 and 2.4 the electromagnetic parameters are extracted from measurements performed on paraffin single layers loaded with PSrAl or CSrCoTi powder. It is observed at Fig. 5, top row, that real and imaginary parts of permittivity ε_r are much higher for CSrCoTi material than for PSrAl material. Reversely the dielectric losses are much lower. Regarding permeability, bottom row, it is significantly higher for CSrCoTi, as well as corresponding magnetic losses. A relative maximum is observed at 8.8 GHz in imaginary part and magnetic loss factor for CSrCoTi, and around 11.6 GHz for PSrAl. In both cases it is attributed to ferromagnetic resonance phenomenon.

As shown in Fig. 6a, the attenuation constant α given by equation (1) follows the increase of dielectric and magnetic losses depicted in Fig. 5.

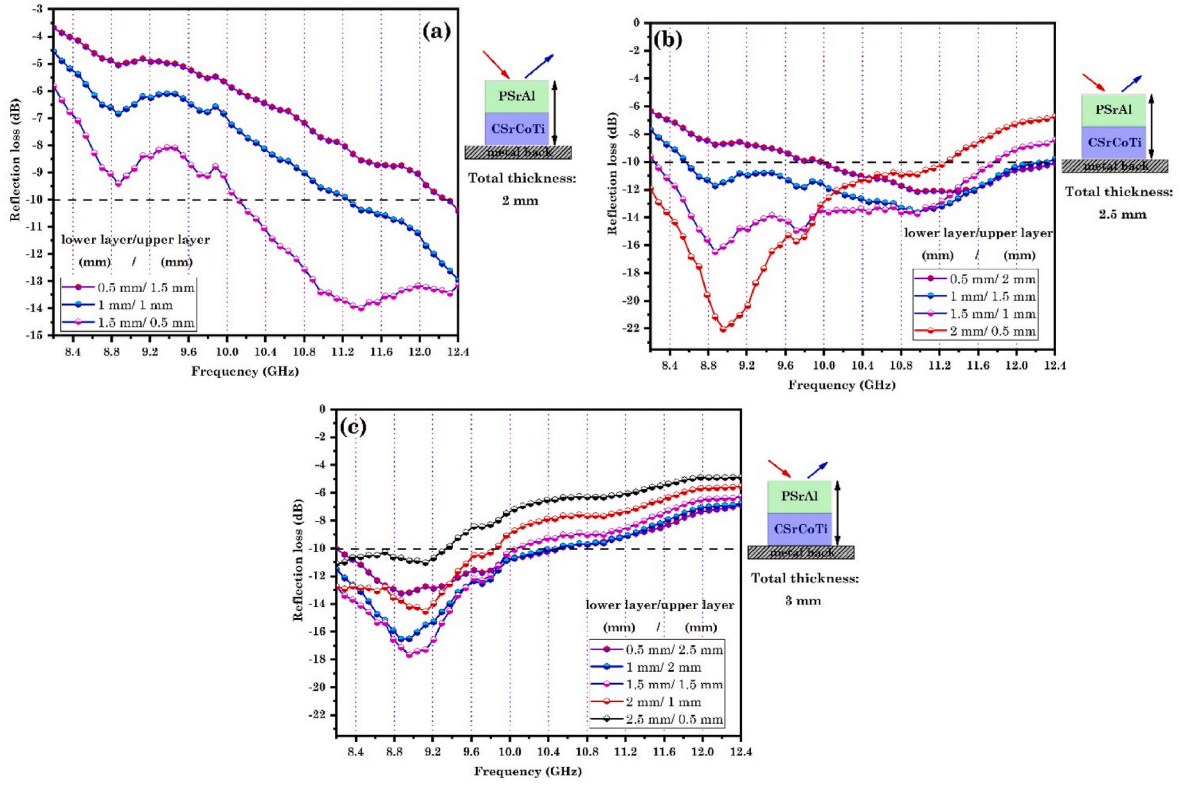

Fig. 8. Reflection loss curves versus frequency of bi-layer samples with total thickness of, a) 2 mm, b) 2.5 mm and c) 3 mm.

$$\alpha = \frac{2\pi}{c}\sqrt{2\mu'\varepsilon'}\sqrt{\frac{\mu''\varepsilon''}{\mu'\varepsilon'} - 1 + \sqrt{\left(\frac{\mu''}{\mu'}\right)^2 + \left(\frac{\varepsilon''}{\varepsilon'}\right)^2 + \left(\frac{\mu''\varepsilon''}{\mu'\varepsilon'}\right)^2 + 1}} \quad (1)$$

On the other hand, the eddy current loss coefficient C_o defined by equation (2) is shown in Fig. 6b.

$$C_0 = \mu''\mu'^{-2}f^{-1} = 2\pi\mu_0\sigma d^2 \quad (2)$$

For both samples $C_o > 0$ as μ" > 0 in Fig. 5e, and is roughly constant above 10 GHz. Assuming that eddy current losses are responsible for the magnetic losses, the C_0 values remain constant versus the frequency [15], as shown in Fig. 6b. It has been also noted that dips are present in both Co and α curves at ferromagnetic resonance frequencies of 11.6 and 8.8 GHz for respectively PSrAl and CSrCoTi single layer samples.

Fig. 6c and d shows the Cole-Cole (CC) representation of the permittivity for each sample analyzed in Fig. 5. The imaginary part noted ε" is represented versus the real part ε', the frequency being an implicit variable.

For each sample a series of circles or semicircles are observed. There are typical of interfacial polarization effects occurring in the nanocomposite. Each interface between hexaferrite powder and neat paraffin is the site of accumulation of polarized charges, while neat paraffin separating hexaferrite inclusions act as an electrical capacitor. The resulting distributed RC network is responsible for the formation of (semi-) circles in the Cole-Cole representation [25]. However, circles are deformed with respect to perfect hemi-circles associated to RC parallel circuits in impedance spectroscopy theory. The deformation of the circles is associated to distributed circuits having different time constants [26,27], and mimicking the dispersive and disordered nature of the material, along with spatial inhomogeneity, dipole polarization, as will be illustrated later in Fig. 10 concluding the paper. The comparison of CC plots reveals that CSrCoTi (Fig. 6c) shows more expanded circles indicating more disorder in the composite system, and interfacial polarization associated to crochet-ball structure.

3.5. Microwave absorption in single layers

Return losses (*RL*) associated to Salisbury configuration, i.e. when the sample layer is backed by a metallic plate, evaluates the attenuation capability of a material: if *RL* is minimized, the signal is absorbed and no signal is reflected back towards input interface of the absorber. The reflection coefficient depends on the input impedance Z_{in} in Salisbury configuration [28]:

$$RL = 20\ log_{10}\left(\frac{Z_{in} - Z_O}{Z_{in} + Z_O}\right) \quad (3)$$

$$Z_{in} = \sqrt{\frac{\mu}{\varepsilon}}\,Z_o\ tanh(\gamma\, d\,) \quad (4)$$

$$\text{where} \quad \gamma = j\,2\,\pi\,f\,\sqrt{\varepsilon\,(\,1 - j\ \tan\delta_\varepsilon)\,\mu\,\left(1 - j\,tan\delta_\mu\right)}\Big/\,c_O \quad (5)$$

c_o is the light velocity in air, Z_o is the 377 Ohms free-space impedance, *f* is the frequency, *d* is the thickness of the layer and ε, μ, $\tan\delta_\varepsilon$, $\tan\delta_\mu$ are measured permittivity, permeability and associated loss tangent factors given in Fig. 5, respectively.

Equations (3) and (4) reveals that when the imaginary part of Z_{in} cancels, *RL* is minimum and absorption is maximum: this situation appears at frequencies f_o for thicknesses *d* that are multiples of a quarter wavelength λ/4:

$$d = n\frac{\lambda}{4} = n\ C_O\Big/\left(4\,f\sqrt{\varepsilon\mu}\right) \rightarrow f_O = n\ c_o\Big/\left(d\,4\,\sqrt{\varepsilon\mu}\right) \quad (6)$$

Fig. 7 illustrates very well equation (6). The contour maps (top row) are drawn by inserting measured values for ε and μ into equations (4) and (5) giving the input impedance, and varying the frequency from 8 to 12.4 GHz and *d* from 0 mm to 3 mm. The normalized impedance Z_{in}/Z_o contour maps in Fig. 7 (a, b) show a value close to 1 corresponding to matching and maximal absorption function of thickness *d* and

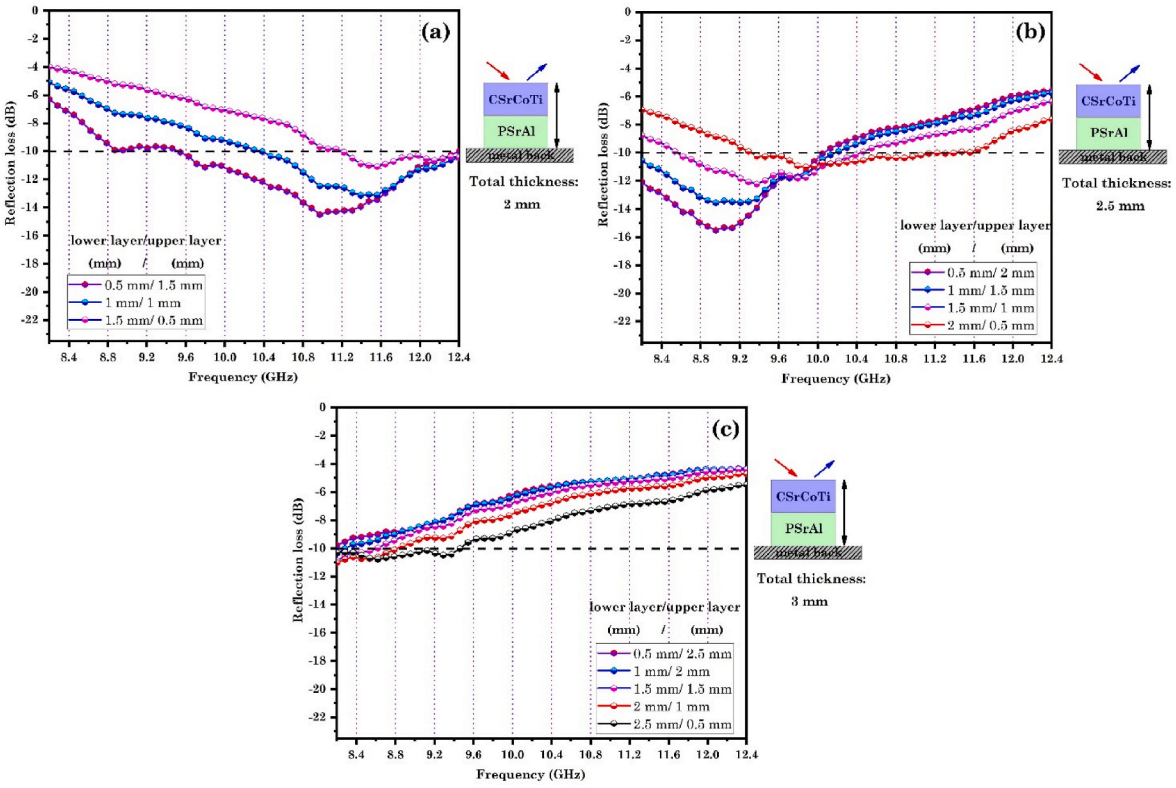

Fig. 9. Reflection loss curves versus frequency of bi-layer samples with total thickness of, a) 2 mm, b) 2.5 mm and c) 3 mm.

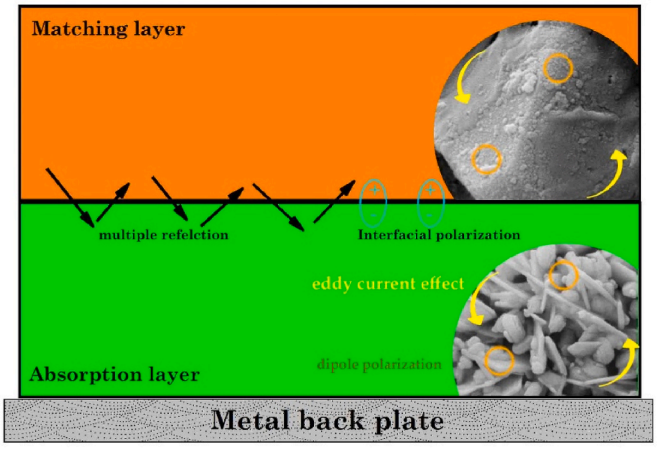

Fig. 10. Mechanisms involved in attenuation/absorption process.

frequency, by virtue of (6). Thicknesses and frequencies where Z_{in}/Z_o are closest to unity are represented by green areas in the maps, going from 8 GHz for $d = 2.5$ mm to 12.4 GHz for $d = 2.0$ mm.

A good absorber must achieve $RL < -10$ d B. This criterion is reached at $d = 2.5$ mm in both samples, see Fig. 7c and d. Best minimum value of RL = −12 dB is observed at 11.6 GHz with an effective absorption bandwidth (EAB) equal to 1.9 GHz for sample PSrAl, while for sample CSrCoTi RL reaches −17.9 dB at 9 GHz with associated EAB equal to 2 GHz, showing thus the best performance for single layer absorber.

3.6. Microwave absorption capability in bilayers

CSrCOTi and PSrAl material layers, can be combined into 2 bilayer configurations. Configuration 1 considers PSrAl material as upper layer

Table 1
Performances for the two bilayer configurations as well as the single layer ones.

Total thickness (mm)	Lower layer/ upper layer (mm)	f_o (GHz)	| RL | (dB)	EAB (GHz)	FOM = RL x EAB
Configuration n°1: Bilayer of Fig. 8					
Upper layer: PSrAl/lower layer: CSrCoTi					
2	0.5/1.5	8.9	5	/	/
	1/1	8.9	7	/	/
	1.5/0.5	11.4	13.5	2.3	31.5
2.5	0.5/2	11.4	12	2.4	28.8
	1/1.5	11.4	13	3.8	49.4
	1.5/1	8.9	18	3.8	68.4
	2/0.5	**8.9**	**22**	**3.2**	**70.4**
3	0.5/2.5	8.9	13.5	2.4	32.4
	1/2	9.0	16	2.4	38.4
	1.5/1.5	8.9	17	2	34
	2/1	9.2	14	1.8	25.2
	2.5/0.5	8.9	10	1.3	13
Configuration n°2: Bilayer of Fig. 9					
Upper layer: CSrCoTi/lower layer: PSrAl					
2	0.5/1.5	11.2	15	2.8	42
	1/1	11.6	12	2	24
	1.5/0.5	11.6	11	1.2	13.2
2.5	**0.5/2**	**9.0**	**16**	**2**	**32**
	1/1.5	9.1	13	2	26
	1.5/1	9.6	12	2	24.7
	2/0.5	10.8	11	2.4	24.2
3	0.5/2.5			/	
	1/2			/	
	1.5/1.5			/	
	2/1			/	
	2.5/0.5			/	
	0.5/1.5	8.9	10	1.2	12
Monolayer of Fig. 7					
Best performances					
2.5 (CSrCoTi)		11.6	12	1.9	12
2.5 (PSrAl)		**9**	**17.9**	**2**	**35.8**

stacked with CSrCoTi material as bottom layer backed by a metallic plane in order to reproducing the RCS Salisbury configuration. The signal is incident to upper PSrAl layer. In configuration 2 the order of upper and lower layers is reverted, and signal is incident to CSrCoTi layer. Fig. 8 presents *RL* curves simulated using Matlab software for configuration 1, while Fig. 9 shows simulations for configuration 2. For both configurations, three total thicknesses are considered: 2, 2.5 and 3 mm.

Table 1 gives the performances for the two bilayer configurations as well as the single layer ones discussed in Section 3.5. EAB is the effective absorption bandwidth, corresponding to RL < - 10 dB. The figure of merit FOM = EAB x |RL|; it means that we want the lowest reflection losses RL over the highest possible frequency range.

From Table 1 it is concluded that bilayer configuration n°1 having upper layer PSrAl shows the best performances in terms of RL and EAB, since a FOM as high as 70.4 is obtained for a 2.5 mm global thickness, spreading into 0.5 mm for upper PSrAl layer followed by CStCoTi layer of thickness 2 mm. The upper PSrAl layer having the lowest dielectric constant acts thus as matching layer favoring the penetration of the signal in the bilayer, while lower CStCoTi layer act as absorbing layer.

Fig. 10 summarizes the different mechanisms involved in the attenuation process, as discussed in this section and in section 3.4 and Fig. 6c, d.

4. Conclusions

In this research, two distinct magnetic powders with $SrFe_{10}Al_2O_{19}$ (PSrAl) and $SrFe_{10}CoTiO_{19}$ (CSrCoTi) chemical formulas with crochet ball like and polyginal pyramidal shapes were synthesized through the solvothermal method. The single layer absorber samples, which contain 20 wt% of PSrAl (RL: 12 dB, EAB: 1.9 GHz, thickness: 2.5 mm) and CSrCoTi (RL: 17.9 dB, EAB: 2 GHz, thickness: 2.5 mm), exhibit moderate microwave absorption features. The resonance frequency peak of a sample with PsrAl and CSrCoTi powders is located around 11.6 GHz and 8.8 GHz, respectively. By architecting a bi-layer absorber in which PsrAl powder is placed in the matching layer with a 0.5 mm thickness and CSrCoTi powder is placed in the absorbing layer with a 2 mm thickness, we reached the lowest reflection loss value of −22 dB with a EAB = 3.1 GHz. The major criteria for improving the absorption feature were tuning the filler content composition, morphological characteristics, and layer arrangement. It is possible to improve the interfacial polarization, improve impedance matching, and ultimately increase the reflection loss properties by overlapping the ferromagenetic resonance peaks, generating synergistic effects across layers, and multiscattering the waves between particles.

Declaration of competing interest

The authors declare that they have no known competing financial interests or personal relationships that could have appeared to influence the work reported in this paper.

Acknowledgment

The authors extend their appreciation to the Deanship of Scientific Research at King Khalid University, Saudi Arabia for funding this work through the Research Group Program under grant no. R.G.P 2/125/43.

References

[1] Y. Cao, A. Mustafa Mohamed, M. Abdollahzadeh, I. Huynen, Rational design of CoNi@C-BTC/rGO nanocomposite coated with PEDOT polymer towards enhancing the microwave absorption in X-band frequency, J. Alloys Compd. 862 (2021), 158371.

[2] L. Deng, R. Shu, J. Zhang, Fabrication of ultralight nitrogen-doped reduced graphene oxide/nickel ferrite composite foams with three-dimensional porous network structure as ultrathin and high-performance microwave absorbers, J. Colloid Interface Sci. 614 (2022) 110–119.

[3] J. Xu, R. Shu, J. Shi, Synthesis of tetragonal copper-nickel ferrite decorated nitrogen-doped reduced graphene oxide composite as a thin and high-efficiency electromagnetic wave absorber, Colloids Surf. A Physicochem. Eng. Asp. 648 (2022), 129411.

[4] J.B. Kim, Design of Salisbury screen absorbers using dielectric lossy sheets, in: Proceedings of the 2011 IEEE International Conference on Microwave Technology & Computational Electromagnetics, Beijing, China, May 2011, pp. 1–2, 22–25.

[5] J.H. Oh, K.S. Oh, C.G. Kim, C.S. Hong, Design of radar absorbing structures using glass/epoxy composite containing carbon black in X-band frequency ranges, Compos. Part B 35 (2004) 49–56.

[6] J.B. Kim, S.W. Lee, C.G. Kim, Comparison study on the effect of carbon nano materials for single-layer microwave absorbers in X-band, Compos. Sci. Technol. 68 (2008) 2909–2916.

[7] M. Jafarian, S.F. Kashani Bozorg, A.A. Amadeh, Y. Atassi, Hierarchical brain-coral-like structure (3D) vs rod-like structure (1D): effect on electromagnetic wave loss features of $SrFe_{12}O_{19}$ and $CoFe_2O_4$, Ceram. Int. 47 (2021) 30448–30458.

[8] P.M. Raj, D. Mishra, H. Sharma, S. Swaminathan, R. Tummala, Chap. 1, Nanomagnetic materials and structures, and their applications in integrated rf and power modules, Nanomagnetism (2014) 1–29.

[9] F. Qin, F, H.X. Peng, N.Y. Pankratov, M. Phan, L.V. Panina, M. Ipatov, V. Zhukova, A. Zhukov, J. Gonzalez, Exceptional electromagnetic interference shielding properties of ferromagneticmicrowires enabled polymer composites, J. Appl. Phys. 108 (2010), 044510.

[10] X. Ma, Q. Zhang, Z. Luo, X. Lin, G. Wu, A novel structure of ferroaluminum-based sandwich composite for magnetic and electromagnetic interference shielding, Mater. Des. 89 (2016) 71–77.

[11] K. Singh, A. Ohlan, A. Bakhshi, S. Dhawan, Synthesis of conducting ferromagnetic nanocomposite with improved microwave absorption properties, Mater. Chem. Phys. 119 (2010) 201–207.

[12] D. Micheli, R. Pastore, A. Vricella, M. Marchetti, Matter's electromagnetic signature reproduction by graded-dielectric multilayer assembly, IEEE Microwave Theory and Techn 65 (8) (2017) 2801–2809.

[13] P. Shital Patangrao, High frequency millimetre wave absorbers derived from polymeric nanocomposites, Polymer 84 (2016) 398–419.

[14] Jean-Michel Thomassin, Polymer/carbon-based composites as electromagnetic interference (EMI) shielding materials, Mater. Sci. Eng. R Rep. 74 (7) (2013) 211–232.

[15] F. Wen, F. Zhang, Z. Liu, Investigation on microwave absorption properties for multiwalled carbon nanotubes/Fe/Co/Ni nanopowders as lightweight Absorbers, J. Phys. Chem. C 115 (2011) 14025–14030.

[16] Z. Wang, G.L. Zhao, Electromagnetic wave absorption of multi-walled carbon nanotube–epoxy composites in the R band, J. Mater. Chem. C 2 (2014) 9406–9411.

[17] S. Chakraborty, N. Saxena Bhattacharyy, S. Bhattacharyy, Single layered wide bandwidth nanosized strontium hexa-ferrite filled LLDPE absorber in X-band, Progr. Electromagn. Res. B 71 (2016) 137–152.

[18] S. Dong, C. Lin, X. Meng, One-pot synthesis and microwave absorbing properties of ultrathin SrFe12O19 nanosheets, J. Alloys Compd. 783 (2019) 779–784.

[19] N. Chen, G. Mu, X. Pan, K. Gan, M. Gu, Microwave absorption properties of SrFe12O19/ZnFe2O4composite powders, Mater. Sci. Eng. B 139 (2007) 256–260.

[20] J. Luo, P. Shen, W. Yao, C. Jiang, J. Xu, Synthesis, characterization, and microwave absorption properties of reduced graphene oxide/strontium ferrite/polyaniline nanocomposites, Nanoscale Res. Lett. 11 (2016) 141.

[21] N. Chen, G. Mu, X. Pan, K. Gan, M. Gu, Microwave absorption properties of SrFe12O19/ZnFe2O4 composite powders, Mater. Sci. Eng. B 139 (2007) 256–260.

[22] M. Jafarian, S.S.S. Afghahi, Y. Atassi, M. Salehi, Insights on the design of a novel multicomponent microwave absorber based on SrFe10Al2O19 and Ni0.5Zn0.5Fe2O4/MWCNTs/polypyrrole, J. Magn. Magn Mater. 471 (2019) 30–38.

[23] D. Xu, M. Jafarian, S.S.S. Afghahi, Y. Atassi, R. Al-Qassar Bani Al-Marjeh, Remarkable microwaveaabsorptipon efficiency of low loading ratio of Ni0.25Co0.25Ti0.5Fe2O4/SrCoTiFe10O19/Cu composite coated with polyprrole within polyurethane matrix, Mater. Res. Express 7 (2020), 016103.

[24] X. Zheng, Y. Li, X. Fun, Design of efficient microwave absorbers based on cobalt-based MOF/SrFe10CoTiO19/carbon nanofibers nanocomposite, J. Supercond. Nov. Magnetism 33 (2020) 2745–2751.

[25] R. Jaiswar, F. Mederos-Henry, S. Hermans, J.P. Raskin, I. Huynen, Nonlinear electrical transport in Fe3O4-decorated graphene nanoplatelets, J. Phys. Appl. Phys. 54 (2021), 065304.

[26] M. Jafarian, S.F. Kashani Bozorg, A.A. Amadeh, Y. Atassi, Nano-architectured NiO shell vs 3D microflowers morphology toward enhancement of magneto-electric loss in mesoporous magneto-electric composite, Ceram. Int. 47 (2021) 20595–20609.

[27] M. Jafarian, S.F. Kashani Bozorg, A.A. Amadeh, Y. Atassi, Boosted microwave dissipation performance via integration of magneto/dielectric particles with hierarchical 3D morphology in bilayer absorber, J. Magn. Magn Mater. 539 (2021), 168363.

[28] R. Shu, J. Xu, Z. Wan, X. Cao, Synthesis of hierarchical porous nitrogen-doped reduced graphene oxide/zinc ferrite composite foams as ultrathin and broadband microwave absorbers, J. Colloid Interface Sci. 608 (2022) 2994–3003.